Transparent Co_3FeO_x Film Passivated $BiVO_4$ Photoanode for Efficient Photoelectrochemical Water Splitting①

FANG Ming[a, b] QIN Qi[b]
CAI Qian[b] LIU Wei[b②]

[a] (*Fujian Normal University, Fuzhou* 350007, *China*)

[b] (*CAS Key Laboratory of Design and Assembly of Functional Nanostructures, Fujian Provincial Key Laboratory of Nanomaterial, Fujian Institute of Research on the Structure of Matter, Chinese Academy of Sciences, Fuzhou* 350002, *China*)

ABSTRACT Photoelectrochemistry that use semiconductors to absorb sunlight for water splitting provides an effective method for the development of renewable hydrogen energy in the future. In this paper, a transparent and highly-efficient cobalt-iron oxide (Co_3FeO_x) nano-film was fabricated through hydrothermal method by directional adjustment of atomic ratio to promote the kinetics of $BiVO_4$ (BVO) photoanode water oxidation. As a result, the Co_3FeO_x-modified BVO photoanode (Co_3FeO_x/BVO) exhibits an impressive photocurrent density of 4.0 mA cm^{-2} at 1.23 V versus reversible hydrogen electrode (RHE), approximately 2.17-fold higher than that of bare BVO, as well as a cathodically shifted onset potential of 320 mV. Transparent catalyst nanolayer structure is clarified by ultraviolet-visible spectroscopy. In addition, the Co_3FeO_x/BVO photoanode has better stability, and there is no obvious activity degradation after 10 hours of reaction. This strategy provides a broad prospect for the use of water oxidation co-catalyst to achieve effective water splitting.

Keywords: photoelectrochemical water splitting, bismuth vanadate, co-catalyst, cobalt-iron oxide;
DOI: 10.14102/j.cnki.0254-5861.2011-3162

1 INTRODUCTION

Photoelctrochemical (PEC) for water splitting has great potential in the production of sustainable hydrogen fuel and climate change issues[1-3]. The water splitting process consists of two different half reactions, namely the oxygen evolution reaction (OER) of the positive electrode and the hydrogen evolution reaction (HER) of the negative electrode[4-7]. Therefore, the development of an efficient photoanode is an essential part of PEC water splitting. Effective photoanode requires excellent light response, effective charge separation and long-term stability in an aqueous medium and does not react with the aqueous solution[8-10]. Among various available metal oxide semi-conductors, bismuth vanadate is among the most promising materials fit for photoanode semiconductors because of proper conduction band edge position and narrow band gap[11, 12]. However, due to serious surface reorganization and slow water oxidation kinetics, practical photocurrent densities of the pure BVO are much smaller than the theoretical value (7.5 mA cm^{-2} at AM 1.5 G)[13, 14]. Therefore, how to significantly improve the kinetics of BVO photoanode OER water oxidation still faces huge challenges. Lately, many efforts such as element doping[15-17], cocatalyst deposition[18-20], heterojunction construction[21-23] and nanostructured control[24-26] have been made to improve the kinetics of BVO photoanode. Among various methods, the introduction of OER catalyst can accelerate water oxidation reaction and consumption of photogenerated holes, thereby inhibiting the recombination of photogenerated carriers[27, 28]. Recently, because of their particular electronic structure and orbital, nickel- and cobalt-based materials have obtained wide applications in promising OER non-noble metal catalysts, particularly layered double hydroxides (LDH) and

Received 26 February 2021; accepted 26 March 2021

① This research was supported by the National Natural Science Foundation of China (Nos. 61674152 and 51902309) and the Natural Science Foundation of Fujian Province (No. 2018J05097)

② Corresponding author. E-mail: liuw@fjirsm.ac.cn

metal oxides with Fe and Co species[29-33]. However, the disadvantages of nickel- and cobalt-based LDH are poor electronic conductivity, which hinders the catalytic activity of the catalyst. As we all know, doping Fe in NiOOH may increase the catalytic activity of OER[34-36] because this doping possibly affects NiOOH's local electronic structure[37], and the addition of Fe heteroatoms may gain active site points and reinforce the charge transfer kinetics between Ni and Fe sites[38]. In addition, OER catalyst can also improve the stability of the photoanode. The uniform load on the surface of the photoanode by blocking the direct contact with the electrolyte, which can effectively protect the photoanode from photocorrosion[39].

Inspired by the above analysis, in the research, we propose one easy and efficient hydrothermal immersion synthesis method, which can construct the ultrathin and transparent CoFe-based oxide nanolayers on the BVO photoanode as a water oxidation catalyst to enhance the water decomposition ability of PEC. The best OER activity is achieved by adjusting the ratio of Co/Fe atoms. As a result, under the AM 1.5G sunlight, the photocurrent density of BVO photoanode modified with the Co/Fe atomic ratio of 3:1 catalyst reached 4.0 mA^{-2} at 1.23 V versus RHE, which was 2.17 times that of the original BVO. Moreover, the photoanode also shows satisfactory stability under high current density and could achieve stable water splitting within 10 hours, without a significant drop in photocurrent density, mainly originating from the protection of ultrathin Co_3FeO_x film. Detailed experimental research and PEC test show that proper Fe element doping can fine-tune the valence and electronic state of Co element, thereby exposing more active sites. In this work, the efficient and stable Co_3FeO_x/BVO photoanode provides new insights into the metal oxide co-catalyst.

2 EXPERIMENTAL

2. 1 Synthesis of BVO films

The BVO film used our previous method. First, 0.13 mol/L tartaric acid aqueous solution was perepared, then 5 mL acetic acid was added and stirred for 10 minutes, and nitric acid (76wt%, Sigma-Aldrich) was added to adjust PH to 2. Next, 8.9×10^{-2} mol/L bismuth nitrate pentahydrate (98%, Sigma-Aldrich) was added until dissolution. After that, a three-electrode electrodeposition method was used, with the bias voltage kept at 2.6V and the electroplating performed for 40 minutes. Finally, 0.132 mmol $VO(acac)_2$ (98%, Sigma-Aldrich) and the bismuth precursor thin-film electrode were annealed in the air at 500 ℃ for 2 hours. Excessive bismuth oxide was soaked and removed in 1 mol/L NaOH solution.

2. 2 Synthesis of Co_xFe_yO co-catalyst deposition on BVO films

The Co_xFe_yO co-catalysts were deposited using a hydrothermal method. In a typical procedure, a predetermined amount of 2.0 mmol cobalt nitrate hexahydrate and ferric nitrate nonahydrate are added to 50 mL of deionized water. Then, the ratio of Co^{2+} and Fe^{3+} was adjusted to 4:0, 3:1, 2:2, 1:3 and 0:4 for comparison. Next, 2.24 g of urotropine was added to the mixed solution. Finally, it was kept in a Teflon-lined stainless-steel autoclave at 90 ℃ for 2 h, cooled to room temperature and rinsed with deionized water for drying, and stored under vacuum for later testing.

3 RESULTS AND DISCUSSION

The fabrication process of Co_3FeO_x/BVO photoanode is illustrated in Fig. 1a. In detail, the BVO nanoarray synthetic onto a fluorine-doped tin oxide (FTO) by electrodeposition and chemical vapor deposition (CVD) method in our recent study[40-42]. Afterwards, Co_3FeO_x film deposits on BVO photoanode by the hydrothermal method. Briefly, $Co(NO_3)_2$ $6H_2O$ and $Fe(NO_3)_3$ $9H_2O$ needed to be dissolved in 40 mL of DI water with a 3:1 stoichiometric ratio of Co^{2+} and Fe^{3+}. Then 2.24 g hexamethylenetetramine and 1.5 mmol of triethanolamine (TEA) were added to the mixture under stirring. Finally, the above solution was kept at 90 ℃ for 2 h in a Teflon-lined stainless-steel autoclave. The structure diagram is shown in Fig. 1b. Upon illumination, photogenerated holes can be transferred from the conduction band of BVO to the ultrathin Co_3FeO_x film because ultrathin structure could facilitate the holes migration and effectively restrain the charge recombination. Moreover, Co element can serve as conductive and reactive stable host that can reinforce Fe active site activity. The holes can quickly migrate to the catalyst layer and participate in the water oxidation reaction owing to its rapid water oxidation kinetics and lower onset potential. Simultaneously, the electrons migrate to the Pt electrode where H^+ ions are reduced to from H_2. Owing to the more efficient charge separation efficiency and more photogenerated holes accumulation, the higher OER performance is achieved by Co_3FeO_x coating,

which is confirmed by higher photocurrent density (Fig. 4a). The presence of Co_3FeO_x can quickly transfer photo-generated holes from BVO to its outer layer, where metal active sites can utilize these holes. The Co species considered to be the active site can accept the holes generated by BVO and be oxidized to Co_3^+. The resulting high-valent Co species can effectively oxidize water to generate O_2.

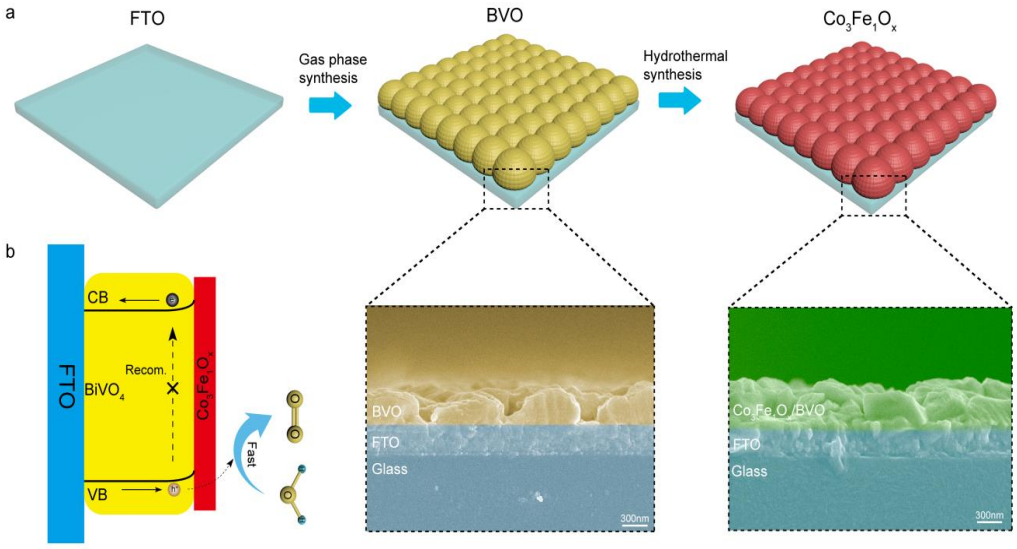

Fig. 1. (a) Synthetic process of Co_3FeO_x/BVO photoanode. (b) Structure schematic of Co_3FeO_x/BVO

The BVO photoanode crystal structure was characterized by SEM and TEM technologies, as shown in Fig. 2. The SEM image (Fig. 2a and Fig. S1, ESI) shows that BVO crystalline is tightly connected to each other to form a nano-flower-like structure and evenly distributed on the FTO substrate. Furthermore, the transmission electron microscopy (TEM) and high-resolution transmission electron micro-scopy (HRTEM) images (Fig. 2d and Fig. 2e) were also performed. The high-crystalline structure with a lattice spacing of 0.47 nm could be clearly observed, which matches well with the (110) lattice plane of monoclinic scheelite BVO. The coating of Co_3FeO_x catalyst layer was synthesized by the hydrothermal method (Supporting Information, Experimental Section). From SEM picture (Fig. 2b and Fig. S2, ESI) we can see that Co_3FeO_x film uniformly covers the surface of BVO crystal. Additionally, the photoelectric performance of Co_3FeO_x/BVO and BVO photoanode was characterized by ultraviolet-visible spectro-scopy (UV-Vis) (Fig. 2c). Clearly, the position of the edge of the absorption band is basically the same after the deposition of OER co-catalyst compared with pure BVO. It can be concluded that the loading of Co_3FeO_x can not expand or weaken the range of its response to light. Moreover, the high resolution TEM images (Fig. 2d) obviously demonstrate that the surface of BVO nanocrystal is evenly covered with a layer of Co_3FeO_x catalyst with a thickness of about 13 nm. The catalyst layer is closely attached to the surface of BVO, which is conducive to the transfer of surface carriers and improves the water oxidation kinetics of PEC and the stability of photoanode. X-ray diffraction (XRD) was taken for the characterization of the crystal structure and phase in all samples obtained (Fig. 2f). The SEM mapping and energy dispersive X-ray spectroscopy (EDS) pattern of Co_3FeO_x/BVO photoanode are displayed in Fig. S3 and Fig. S4. Due to the trace amount of catalyst layer, no information about Co and Fe elements was detected, which will be further verified by XPS analysis. The peak of SnO_2 on the FTO glass substrate is marked with a heart-shaped symbol. In addition, in these samples, the typical diffraction peak of the monoclinic BVO crystal (JCPDS No. 14-0688) can be well detected. In contrast, no evident peak of Co_3FeO_x in Co_3FeO_x/BVO has been observed, which can be attributed to the amorphous and ultra-thin structure of the catalyst layer.

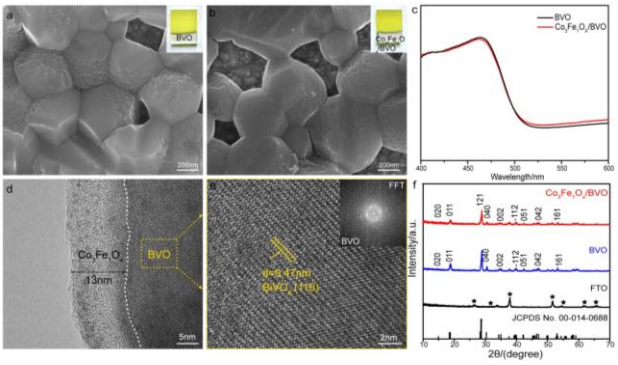

Fig. 2. (a) SEM image of the BVO film. Inset: digital image of BVO photoanode. (b) SEM image of the Co_3FeO_x/BVO film. Inset: digital image of Co_3FeO_x/BVO photoanode. (c) UV-Vis spectra of BVO and Co_3FeO_x/BVO photoanode. (d, e) TEM and high-resolution TEM image of the Co_3FeO_x/BVO film. (f) XRD patterns of the BVO and Co_3FeO_x/BVO films

In order to explore the chemical state and composition of the modified Co_3FeO_x/BVO and BVO photoanode surface, we used X-ray photoelectron spectroscopy (XPS) for characterization. Typical O 1*s*, V 2*p* and Bi 4*f* peaks are found from the XPS spectrum of the two species (Fig. S5, ESI). The characteristic peaks of Bi $4f_{7/2}$ (159 eV), Bi $4f_{5/2}$ (164.2 eV), V $2p_{3/2}$ (516.4 eV) and V $2p_{1/2}$ (524.2 eV) are attributed to Bi^{3+} and V^{5+} in BVO (Fig. 3a and 3b). In particular, the XPS spectrum of Bi and V (Fig. 3a-b) in Co_3FeO_x/BVO is significantly shifted to a higher binding energy than BVO, indicating that the electronic environment around BVO changes with the loading of the catalyst. For the O 1*s* XPS spectrum of Co_3FeO_x/BVO films (Fig. S6, ESI), it is fitted into three peaks. In detail, the peak at 529.9 eV can be assigned to O^{2-} species in the lattice (O_L), that at 531.4 eV results from oxygen vacancies (O_V), and that at 532.4 eV should be attributed to adsorbed hydroxyl group on the surface (O_C)[43]. The Co 2*p* spectrum comprises two major peaks at 781.1 and 796.9 eV, respectively, and the spin orbital split is about 16 eV, corresponding to Co $2p_{3/2}$ and Co $2p_{1/2}$ (Fig. 3c). In addition, two satellite peaks are located at 785.8 and 806.0 eV (denoted as "sat" in Fig. 3c), which are the characteristics of Co^{2+} species. The Fe spectrum (Fig. 3d) contains two primary peaks at 710.6 and 724.5 eV, attributed to Fe $2p_{3/2}$ and Fe $2p_{1/2}$ of Fe^{3+}, respectively. Furthermore, two satellite peaks located at higher binding energies 716.9 and 732.5 eV (denoted as "sat" in Fig. 3d), which can be ascribed to the charge-transfer or shakeup processes associated with Fe^{3+}[44]. These results further indicate the successful synthesis of Co_3FeO_x/BVO photoanode.

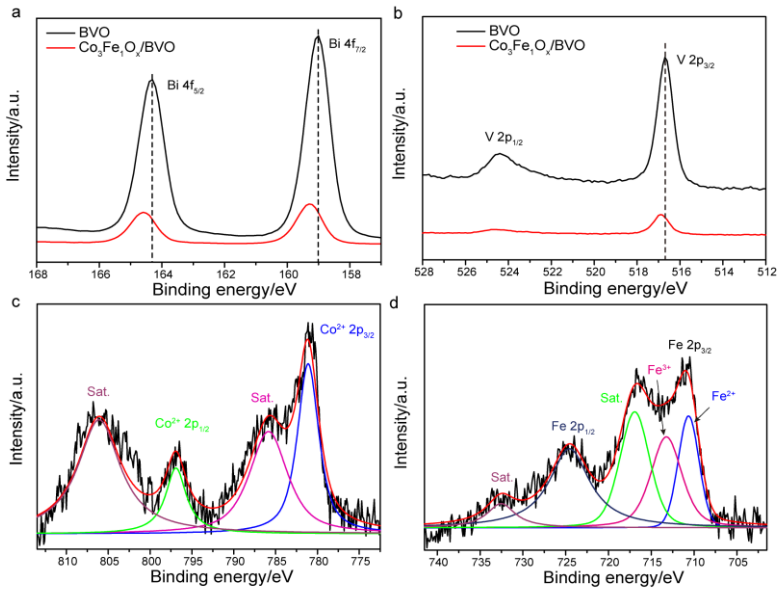

Fig. 3. (a-b) High-resolution XPS spectra for BVO and Co_3FeO_x/BVO: (a) Bi 4*f*, (b) V 2*p*, (c-d) High-resolution XPS spectra of the Co_3FeO_x/BVO film: (c) Co 2*p*, and (d) Fe 2*p*

To investigate the PEC water splitting performance, photocurrent density-potential (J-V) curves of BVO and Co_3FeO_x/BVO photoanodes needed to be documented by 1 mol/L K_3BO_3 electrolyte (pH = 9.5) in AM 1.5 G simulated sunlight (100 mW cm^{-2}). As shown in Fig. 4a, the linear sweep voltammetry (LSV) curve shows that the original BVO film only exhibits a photocurrent density of 1.84 mA cm^{-2} at 1.23 V versus RHE, and also an onset potential of ~0.4 V versus RHE. After loading the Co_3FeO_x layer as co-catalyst, it is gratifying that the photocurrent density was increased by 1.17 times at 1.23V versus RHE, reaching 4.0 mA cm^{-2} (Fig. 4a). Besides, this photocurrent density is better than most of the previously reported BVO electrodes modified by co-catalyst (Table S1, ESI). In addition, compared with pure BVO, it shows a significant cathodic displacement of the starting potential. At the same time, the PEC water oxidation performance of CoPi/BVO was also measured under the same conditions for comparison. Clearly, BVO and Co_3FeO_x/BVO films show a similar onset potential, while Co_3FeO_x/BVO photoanode exhibits the higher current density at a voltage of 1.23 V versus RHE.

For understanding the intrinsic mechanism of improved PEC performance, the incident photon-current conversion efficiency (IPCE) curve for BVO and Co_3FeO_x/BVO electrodes should be assessed at 1.23 V versus RHE (Fig. 4b). Both BVO and Co_3FeO_x/BVO films exhibit photo-current response from 350 to 520 nm, conforming to the UV-vis data (Fig. 2c) at the edge of light absorption. Compared with BVO, Co_3FeO_x/BVO shows great efficiency in the entire wavelength range. The maximum IPCE of Co_3FeO_x/BVO is 41.7%, while the maximum IPCE of original BVO is 21%. Fig. 4c demonstrates the bias photon-to-current efficiency (ABPE) in the sample. The ABPE value of BVO film is 0.28% at 0.7 V, which is gratifyingly that after the Co_3FeO_x catalyst deposited the ABPE value is increased to 1.2% at 0.77 V. The excellent photoelectric properties of the Co_3FeO_x/BVO electrode are caused by the decrease of surface charge recombination, which can be further verified through measuring the chopping transient photocurrent density (Fig. 4d). When the lamp is cycled on or off, an upward current spike will appear, which is caused by the accumulation of holes between the electrode and the electrolyte interface. In this case, the surface state and reaction kinetics of the electrode photoresponse affect the smoothness of the current spike. As shown in Fig. 4b, the pure BVO electrode has a strong spike, indicating the charge recombination caused by the slow water oxidation kinetics on the original BVO surface. In contrast, Co_3FeO_x/BVO has a much smoother peak, suggesting the inhibition of surface modification on the recombination of photogenerated carriers. Moreover, electrochemical impedance spectroscopy (EIS) was measured at 0.7 V versus RHE to further evaluate the reaction kinetic. The EIS Nyquist curves of two photoanodes comprise a semicircle fitted to the series resistance (R_s), charge transfer resistance between electrode surface and electrolyte (R_{ct}) and constant interface phase element (CPE) (Fig. 4e). A smaller diameter reflects the smaller charge-transfer resistance, which is used to compare the electron transfer kinetics. Therefore, the Co_3FeO_x-coating can effectively enhance charge transport capability, thus further improving the performance of water splitting. The photoelectric performance of the electrode is characterized by evaluating the surface charge separation efficiency (η_{sep}) associated with the hole reaching the surface. Sodium sulfite (Na_2SO_3) is used as a hole scavenger. Due to the fast kinetics of SO_3^{2-}, the η trans of SO_3^{2-} oxidation can be assumed to be 100%[45] (see the supporting information section for details). According to the results of Fig. 4f, compared with pure BVO (35%), the η_{sep} of Co_3FeO_x/BVO is as high as 78%, which proves that a good interface is formed with high efficiency photoelectric conversion efficiency between Co_3FeO_x/BVO and BVO. In order to confirm the hydrogen evolution reaction at the Pt electrode as well as oxygen evolution reaction at the Co_3FeO_x/BVO photoanode, the amount of hydrogen and oxygen released was analyzed by gas chromatography (GC) (Fig. 4g). With prolonging light time, the contents of H_2 and O_2 showed a linear increase. The amounts of H_2 and O_2 released after 30 minutes were 43.3 and 20.1 μmol, respectively with the stoichiometric ratio to be about 2:1, which was basically consistent with the theoretical results. Mott-Schottky (MS) was measured in a 1 mol/L potassium borate solution under dark conditions (Fig. 4h). The BVO and Co_3FeO_x/BVO demonstrate the positive slope in MS curves, showing n-type characteristics. Compared with the BVO film, the MS plot of Co_3FeO_x/BVO shows a gentler slope, indicating an increase in carrier concentration after Co_3FeO_x is deposited, which is just in line with the above experimental results. The high stability of photoanode also plays an important role in future practical application. Therefore, we studied the stability of the prepared photoanode. Fig. 4i shows the water oxidation stability of the original BVO and Co_3FeO_x/BVO membrane

PEC in a 1 mol/L potassium borate buffer solution. It can be clearly seen that after 10 hours of stability test, the photocurrent density of BVO dropped to 75.9%. We believe that the photocurrent density degradation of BVO in water oxidation should be attributed to its poor kinetics, leading to the serious recombination of photogenerated electron and hole pairs. In addition, after assembling the catalyst, the stability of BVO photoelectrode is significantly improved. Compared with BVO, the photocurrent density of Co_3FeO_x/BVO maintains 95.5%, indicating the prominent role of Co_3FeO_x cocatalysts in reinforcing the OER activity and stability of BVO photoanodes.

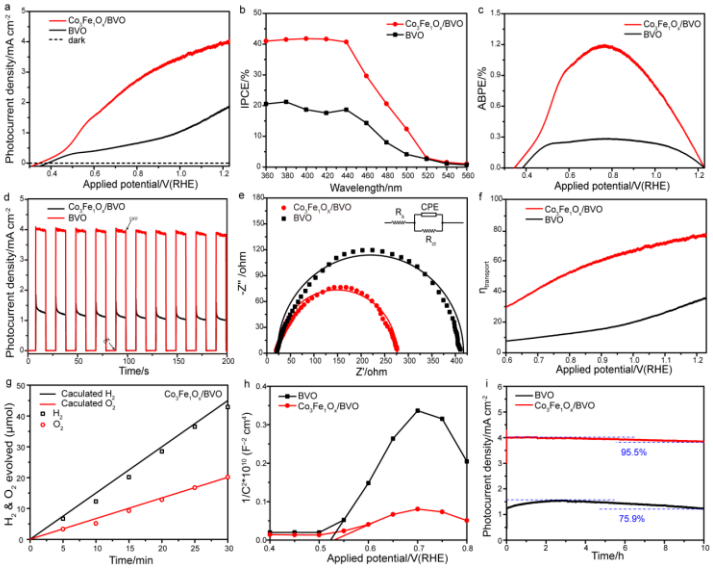

Fig. 4. PEC performance for BVO and Co_3FeO_x/BVO photoanodes. (a) Photocurrent density versus applied potential curves, (b) IPCE curves obtained at 1.23 V versus RHE, (c) ABPE curves, (d) Transient photocurrent density as a function of time under illumination at an applied potential of 1.23 V versus RHE, (e) EIS spectra measured under 1.23 V versus RHE and AM 1.5G illumination (Inset: the equivalent circuit model) (f) Charge transfer efficiency versus applied potential curves. (g) Fluorescence probe measurement of O_2 and H_2 generation from Co_3FeO_x/BVO photoanode. (h) Mott-Schottky plots of BVO, and Co_3FeO_x/BVO photoanodes, (i) photocurrent density versus time curves at 1.23 V versus RHE under AM 1.5 G illumination of the photoanodes. All measurements were performed in a 1 mol/L potassium borate electrolyte (pH 9.5)

4 CONCLUSION

In summary, we have prepared a transparent cobalt-iron oxide layer on the surface of BVO by the hydrothermal method to construct a composite structure photoanode. The Co_3FeO_x/BVO photoanode achieves a remarkable photo-current density of 4.0 mA cm^{-2} at 1.23 V versus RHE by optimizing the proportion of cobalt iron ions, and a low onset potential (~320 mV) for water splitting also achieved. In addition, the Co_3FeO_x/BVO thin film photoanode also showed a more stable photoactivity, and it still maintained a photocurrent density of 95.5% after a 10h stability test. Our research shows that the excellent PEC activity is attributable to the protection of Co_3FeO_x and the inhibition of charge recombination to improve the surface reaction efficiency, as well as the timely consumption of photo-generated holes reaching the surface to improve the overall stability. Our work may provide a promising strategy for improving the PEC performance of BVO photoanode in solar water splitting.

REFERENCES

(1) Gratzel, M. Photoelectrochemical cells. *Nature* **2001**, 414, 338−344.

(2) Nellist, M. R.; Laskowski, F. A. L.; Lin, F.; Mills, T. J.; Boettcher, S. W. Semiconductor-electrocatalyst interfaces: theory, experiment, and applications in photoelectrochemical water splitting. *Acc. Chem. Res.* **2016**, 49, 733−740.

(3) Jiang, C.; Moniz, S. J. A.; Wang, A.; Zhang, T.; Tang, J. Photoelectrochemical devices for solar water splitting-materials and challenges. *Chem. Soc. Rev.* **2017**, 46, 4645−4660.

(4) Moniz, S. J. A.; Shevlin, S. A.; Martin, D. J.; Guo, Z. X.; Tang, J. Visible-light driven heterojunction photocatalysts for water splitting-acritical review. *Energy Environ. Sci.* **2015**, 8, 731−759.

(5) Zhang, H.; Li, L.; Liu, C.; Wang, W.; Liang, P.; Mitsuzak, N.; Chen, Z. Carbon coated alpha-Fe_2O_3 photoanode synthesized by a facile anodic electrodeposition for highly efficient water oxidation. *Electron. Mater. Lett.* **2018**, 14, 348−356.

(6) Huang, J.; Ding, Y.; Luo, X.; Feng, Y. Solvation effect promoted formation of p-n junction between WO_3 and FeOOH: a high performance photoanode for water oxidation. *J. Catal.* **2016**, 333, 200−206.

(7) Tian, T.; Gao, H.; Zhou, X.; Zheng, L.; Wu, J.; Li, K.; Ding, Y. Study of the active sites in porous nickel oxide nanosheets by manganese modulation for enhanced oxygen evolution catalysis. *ACS Energy Lett.* **2018**, 3, 2150−2158.

(8) Kim, T. L.; Choi, M. J.; Jang, H. W. Boosting interfacial charge transfer for efficient water-splitting photoelectrodes: progress in bismuth vanadate photoanodes using various strategies. *Mrs Communications* **2018**, 8, 809−822.

(9) Xu, X. T.; Pan, L.; Zhang, X.; Wang, L.; Zou, J. J. Rational design and construction of cocatalysts for semiconductor-based photo-electrochemical oxygen evolution: a comprehensive Review. *Adv. Sci.* **2019**, 6.

(10) Zhong, D. K.; Choi, S.; Gamelin, D. R. Near-complete suppression of surface recombination in solar photoelectrolysis by "Co-Pi" catalyst-modified W:$BiVO_4$. *J. Am. Chem. Soc.* **2011**, 133, 18370−18377.

(11) Abdi, F. F.; Savenije, T. J.; May, M. M.; Dam, B.; van de Krol, R. The origin of slow carrier transport in $BiVO_4$ thin film photoanodes: a time-resolved microwave conductivity study. *J. Phys. Chem. Lett.* **2013**, 4, 2752−2757.

(12) McDonald, K. J.; Choi, K. S. A new electrochemical synthesis route for a BiOI electrode and its conversion to a highly efficient porous $BiVO_4$ photoanode for solar water oxidation. *Energy Environ. Sci.* **2012**, 5, 8553−8557.

(13) Kim, T. W.; Choi, K. S. Nanoporous $BiVO_4$ photoanodes with dual-layer oxygen evolution catalysts for solar water splitting. *Science* **2014**, 343, 990−994.

(14) Zhou, M.; Bao, J.; Xu, Y.; Zhang, J.; Xie, J.; Guan, M.; Wang, C.; Wen, L.; Lei, Y.; Xie, Y. Photoelectrodes based upon Mo: $BiVO_4$ inverse opals for photoelectrochemical water splitting. *ACS Nano* **2014**, 8, 7088−7098.

(15) Gao, L.; Long, X.; Wei, S.; Wang, C.; Wang, T.; Li, F.; Hu, Y.; Ma, J.; Jin, J. Facile growth of $AgVO_3$ nanoparticles on Mo-doped $BiVO_4$ film for enhanced photoelectrochemical water oxidation. *Chem. Eng. J.* **2019**, 378.

(16) Reddy, C. V.; Reddy, I. N.; Ravindranadh, K.; Reddy, K. R.; Shim, J.; Cheolho, B. Au-doped $BiVO_4$ nanostructure-based photoanode with enhanced photoelectrochemical solar water splitting and electrochemical energy storage ability. *Appl. Surf. Sci.* **2021**, 545.

(17) Nellist, M. R.; Qiu, J.; Laskowski, F. A. L.; Toma, F. M.; Boettcher, S. W. Potential-sensing electrochemical AFM Shows CoPi as a hole collector and oxygen evolution catalyst on $BiVO_4$ water-splitting photoanodes. *ACS Energy Lett.* **2018**, 3, 2286−2291.

(18) Zhang, L.; Reisner, E.; Baumberg, J. J. Al-doped ZnO inverse opal networks as efficient electron collectors in $BiVO_4$ photoanodes for solar water oxidation. *Energy Environ. Sci.* **2014**, 7, 1402−1408.

(19) Zhang, B.; Wang, L.; Zhang, Y.; Ding, Y.; Bi, Y. Ultrathin FeOOH nanolayers with abundant oxygen vacancies on $BiVO_4$ photoanodes for efficient water oxidation. *Angew. Chem. Int. Ed.* **2018**, 57, 2248−2252.

(20) Zhang, P.; Li, S. Q.; Guo, Z. J.; Zhang, C. Q.; Yang, C. Q.; Han, S. S. Investigation on purification of α-Fe_2O_3 from zinc smelting iron slag by superconducting HGMS technology. *Progress in Superconductivity and Cryogenics* **2018**, 20, 16−19.

(21) Bai, S.; Chu, H.; Xiang, X.; Luo, R.; He, J.; Chen, A. Fabricating of Fe_2O_3/$BiVO_4$ heterojunction based photoanode modified with NiFe-LDH nanosheets for efficient solar water splitting. *Chem. Eng. J.* **2018**, 350, 148−156.

(22) Xie, M.; Fu, X.; Jing, L.; Luan, P.; Feng, Y.; Fu, H. Long-lived, visible-light-excited charge carriers of TiO_2/$BiVO_4$ nanocomposites and their unexpected photoactivity for water splitting. *Adv. Energy Mater.* **2014**, 4.

(23) Li, D.; Liu, Y.; Shi, W.; Shao, C.; Wang, S.; Ding, C.; Liu, T.; Fan, F.; Shi, J.; Li, C. Crystallographic-orientation-dependent charge separation of $BiVO_4$ for solar water oxidation. *ACS Energy Lett.* **2019**, 4, 825−831.

(24) Han, H. S.; Shin, S.; Kim, D. H.; Park, I. J.; Kim, J. S.; Huang, P. S.; Lee, J. K.; Cho, I. S.; Zheng, X. Boosting the solar water oxidation performance of a $BiVO_4$ photoanode by crystallographic orientation control. *Energy Environ. Sci.* **2019**, 12, 1427−1427.

(25) Li, M.; Yu, S.; Huang, H.; Li, X.; Feng, Y.; Wang, C.; Wang, Y.; Ma, T.; Guo, L.; Zhang, Y. Unprecedented eighteen-faceted BiOCl with a ternary facet junction boosting cascade charge flow and photo-redox. *Angew. Chem. Int. Ed.* **2019**, 58, 9517−9521.

(26) Kuang, P.; Zhang, L.; Cheng, B.; Yu, J. Enhanced charge transfer kinetics of Fe_2O_3/CdS composite nanorod arrays using cobalt-phosphate as

cocatalyst. *Appl. Catal., B* **2017**, 218, 570−580.

(27) Ding, C.; Shi, J.; Wang, Z.; Li, C. Correction to photoelectrocatalytic water splitting: significance of cocatalysts, electrolyte, and interfaces. *ACS Catal.* **2017**, 7, 1706−1706.

(28) Wang, S.; Wang, T.; Wang, X.; Deng, Q.; Yang, J.; Mao, Y.; Wang, G. Intercalation and elimination of carbonate ions of NiCo layered double hydroxide for enhanced oxygen evolution catalysis. *Int. J. Hydrogen Energy* **2020**, 45, 12629−12640.

(29) Song, F.; Hu, X. Ultrathin cobalt-manganese layered double hydroxide is an efficient oxygen evolution catalyst. *J. Am. Chem. Soc.* **2014**, 136, 16481−16484.

(30) Batchellor, A. S.; Boettcher, S. W. Pulse-electrodeposited Ni–Fe (oxy)hydroxide oxygen evolution electrocatalysts with high geometric and intrinsic activities at large mass loadings. *ACS Catal.* **2015**, 5, 6680−6689.

(31) Zhou, X.; Shen, X.; Xia, Z.; Zhang, Z.; Li, J.; Ma, Y.; Qu, Y. Hollow fluffy Co_3O_4 cages as efficient electroactive materials for supercapacitors and oxygen evolution reaction. *ACS Appl. Mater. Interfaces* **2015**, 7, 20322−20331.

(32) Xu, L.; Jiang, Q.; Xiao, Z.; Li, X.; Huo, J.; Wang, S.; Dai, L. Plasma-engraved Co_3O_4 nanosheets with oxygen vacancies and high surface area for the oxygen evolution reaction. *Angew. Chem. Int. Ed.* **2016**, 55, 5277−5281.

(33) Friebel, D.; Louie, M. W.; Bajdich, M.; Sanwald, K. E.; Cai, Y.; Wise, A. M.; Cheng, M. J.; Sokaras, D.; Weng, T. C.; Alonso-Mori, R.; Davis, R. C.; Bargar, J. R.; Norskov, J. K.; Nilsson, A.; Bell, A. T. Identification of highly active Fe sites in (Ni,Fe)OOH for electrocatalytic water splitting. *J. Am. Chem. Soc.* **2015**, 137, 1305−1313.

(34) Chen, J. Y. C.; Dang, L.; Liang, H.; Bi, W.; Gerken, J. B.; Jin, S.; Alp, E. E.; Stahl, S. S. Operando analysis of NiFe and Fe oxyhydroxide electrocatalysts for water oxidation: detection of Fe^{4+} by mossbauer spectroscopy. *J. Am. Chem. Soc.* **2015**, 137, 15090−15093.

(35) Liu, H.; Wang, Y.; Lu, X.; Hu, Y.; Zhu, G.; Chen, R.; Ma, L.; Zhu, H.; Tie, Z.; Liu, J.; Jin, Z. The effects of Al substitution and partial dissolution on ultrathin NiFeAl trinary layered double hydroxide nanosheets for oxygen evolution reaction in alkaline solution. *Nano Energy* **2017**, 35, 350−357.

(36) Xie, Y.; Wang, X.; Tang, K.; Li, Q.; Yan, C. Blending Fe_3O_4 into a Ni/NiO composite for efficient and stable bifunctional electrocatalyst. *Electrochim. Acta* **2018**, 264, 225−232.

(37) Ren, N.; Wang, A.; Gao, L.; Xin, L.; Lee, D. J.; Su, A. Bioaugmented hydrogen production from carboxymethyl cellulose and partially delignified corn stalks using isolated cultures. *Int. J. Hydrogen Energy* **2008**, 33, 5250−5255.

(38) Lee, D. K.; Choi, K. S. Enhancing long-term photostability of $BiVO_4$ photoanodes for solar water splitting by tuning electrolyte composition. *Nature Energy* **2018**, 3, 53−60.

(39) Qin, Q.; Cai, Q.; Li, J.; Jian, C.; Hong, W.; Liu, W. High quantum efficiency achieved on $BiVO_4$ photoanode for efficient solar water oxidation. *Solar Rrl* **2019**, 3.

(40) Qin, Q.; Cai, Q.; Hong, W.; Jian, C.; Liu, W. Improved hole extraction and durability of $BiVO_4$ photoanode for solar water splitting under extreme pH condition. *Chem. Eng. J.* **2020**, 402.

(41) Wei, S.; Wang, C.; Long, X.; Wang, T.; Wang, P.; Zhang, M.; Li, S.; Ma, J.; Jin, J.; Wu, L. An oxygen vacancy-modulated homojunction structural $CuBi_2O_4$ photocathodes for efficient solar water reduction. *Nanoscale* **2020**, 12, 15193−15200.

(42) Palaniselvam, T.; Shi, L.; Mettela, G.; Anjum, D. H.; Li, R.; Katuri, K. P.; Saikaly, P. E.; Wang, P. Vastly enhanced $BiVO_4$ photocatalytic OER performance by $NiCoO_2$ as cocatalyst. *Adv. Mater. Interfaces* **2017**, 4.

(43) Yin, L.; Adler, I.; Tsang, T.; Matienzo, L. J.; Grim, S. O. Paramagnetism and shake-up satellites in X-ray photoelectron-spectra. *Chem. Phys. Lett.* **1974**, 24, 81−84.

(44) Zhou, L.; Zhao, C.; Giri, B.; Allen, P.; Xu, X.; Joshi, H.; Fan, Y.; Titova, L. V.; Rao, P. M. High light absorption and charge separation efficiency at low applied voltage from Sb-doped SnO_2/$BiVO_4$ core/shell nanorod-array photoanodes. *Nano Lett.* **2016**, 16, 3463−3474.

(45) Seabold, J. A.; Choi, K. S. Efficient and stable photo-oxidation of water by a bismuth vanadate photoanode coupled with an iron oxyhydroxide oxygen evolution catalyst. *J. Am. Chem. Soc.* **2012**, 134, 2186−2192.